

PAPER • OPEN ACCESS

## Detection of individual sub-pixel features in edge-illumination x-ray phase contrast imaging by means of the dark-field channel

To cite this article: Norihito Matsunaga *et al* 2020 *J. Phys. D: Appl. Phys.* **53** 095401

View the [article online](#) for updates and enhancements.



**IOP | ebooks™**

Bringing together innovative digital publishing with leading authors from the global scientific community.

Start exploring the collection—download the first chapter of every title for free.

# Detection of individual sub-pixel features in edge-illumination x-ray phase contrast imaging by means of the dark-field channel

Norihito Matsunaga<sup>1</sup>, Kazuhiro Yano<sup>1</sup>, Marco Endrizzi<sup>2</sup>   
and Alessandro Olivo<sup>2</sup>

<sup>1</sup> Optical Research Laboratory, Nikon Corporation, Yokohama Plant, 471, Nagaodai-cho, Sakaeku, Yokohama City, Kanagawa, Japan

<sup>2</sup> Department of Medical Physics and Biomedical Engineering, University College London, Gower Street, London WC1E 6BT, United Kingdom

E-mail: [Norihito.Matsunaga@nikon.com](mailto:Norihito.Matsunaga@nikon.com) and [m.endrizzi@ucl.ac.uk](mailto:m.endrizzi@ucl.ac.uk)

Received 18 July 2019, revised 31 October 2019

Accepted for publication 22 November 2019

Published 17 December 2019



## Abstract

We report on a direct comparison in the detectability of individual sub-pixel-size features between the three complementary contrast channels provided by edge-illumination x-ray phase contrast imaging at constant exposure time and spatial sampling pitch. The dark-field (or ultra-small-angle x-ray scattering) image is known to provide information on sample micro-structure at length scales that are smaller than the system's spatial resolution, averaged over its length. By using a custom-built groove sample, we show how this can also be exploited to detect individual, isolated features. While these are highlighted in the dark-field image, they remain invisible to the phase and attenuation contrast channels. Finally, we show images of a memory SD card as an indication towards potential applications.

Keywords: x-ray imaging, dark-field imaging, phase-contrast imaging


(Some figures may appear in colour only in the online journal)

## 1. Introduction

Since Wilhelm Röntgen's discovery of x-rays in 1895, x-ray imaging has been widely used for visualizing the internal structure of a sample non-destructively. X-ray phase contrast imaging (XPCI) can obtain high contrast for samples presenting a weak x-ray attenuation, and consequently it has been actively studied over recent years. Several XPCI approaches have been developed to date, including free-space propagation (propagation-based imaging) [1–6], Bonse–Hart interferometry (crystal interferometry) [7–9], analyzer-based imaging (sometimes referred to as diffraction-enhanced imaging) [10–14], Talbot interferometry (grating-based imaging)

[15–22] and edge illumination (EI, sometimes referred to as the coded aperture technique) [23–29]. Details on the various approaches can be found in a series of reviews that were recently published [30–32].

Of these methods, Talbot interferometry and EI have attracted particular attention due to the possibility to implement them with extended sources, which is one of the key requirements in terms of translation from high-end synchrotron facilities to standard laboratories and, ultimately, commercial systems. This paper focuses on EI, mostly because of its implementation not requiring source collimation [24–28], its achromatic properties [33], and its robustness against vibrations and thermal drifts [34]. The edge-illumination technique was first developed in Elettra Synchrotron, Italy in the late 1990s [35]. To date, many experimental results have been reported, mostly based around applications in the biohealth and industrial fields [23–29]. These highlight the technique's

 Original content from this work may be used under the terms of the [Creative Commons Attribution 3.0 licence](https://creativecommons.org/licenses/by/3.0/). Any further distribution of this work must maintain attribution to the author(s) and the title of the work, journal citation and DOI.

potential in terms of application to market, within which hard x-ray dark-field imaging with incoherent sample illumination [26–29] can carve its own niche due to its ability to visualize micro-structures in the sample using laboratory-scale systems, similarly to what has been demonstrated for dark-field imaging in analyzer-based imaging [36] or Talbot interferometry [37].

Dark-field contrast is mainly studied in relation to average microscopic sample features, namely sub-pixel structures averaged over one detector pixel [19, 38–41]. Here, we focus on single, isolated sub-pixel features, demonstrating that these can be detected by the dark-field channel down to sizes below the inherent resolution limits of the imaging system. While this is always possible (e.g., in conventional attenuation-based imaging), so long as a sufficient x-ray statistic is used and small features are simply detected rather than separated from each other, here we show that this is extended significantly further in dark-field compared to both differential phase and attenuation.

A model was developed [42] that expresses the spatial resolution in EI XPCI as the smallest distance between the projected focal spot size and the aperture dimension in the pre-sample mask. This model is based on a system’s total spread function, and it argues the ability to resolve objects that are separated by more than the full width at half maximum of this spread function. As such, it can be used to determine the minimum distance between features at which they can still be detected as separate, but not the detection of individual, isolated objects. This has instead to do with the signal intensity generated by a single isolated, and in this case sub-pixel-sized, object.

## 2. Imaging principle

Figure 1 shows a schematic diagram of the EI XPCI system used in this demonstration experiment. The detector is a Hamamatsu C9732DK CMOS sensor with a pixel size of 50  $\mu\text{m}$ . The x-ray source is a rotating-anode Rigaku MM007 with a molybdenum target. The tube voltage and current settings were 35 kVp and 25 mA, respectively, and the focal spot size is approximately 80  $\mu\text{m}$ . The pre-sample mask, manufactured by Creatv Microtech (Potomac, MD) by electroplating gold on a patterned graphite substrate, had a period of 79  $\mu\text{m}$  and an aperture width of 23  $\mu\text{m}$ . The detector mask was fabricated in the same way and had a period of 98  $\mu\text{m}$  with an aperture width of 29  $\mu\text{m}$ . The distances  $R_1$  between the source and pre-sample mask and  $R_2$  between the pre-sample mask and detector mask were 1.6 m and 0.4 m, respectively, providing approximate harmonic matching of the two pitches. The detector itself is placed a few centimeters downstream of the detector mask, so that the 98  $\mu\text{m}$  period of the latter projects into twice the pixel pitch, in what is often referred to as the skipped EI configuration [43]. This is typically used with indirect conversion detectors to reduce cross-talk between adjacent detector columns.

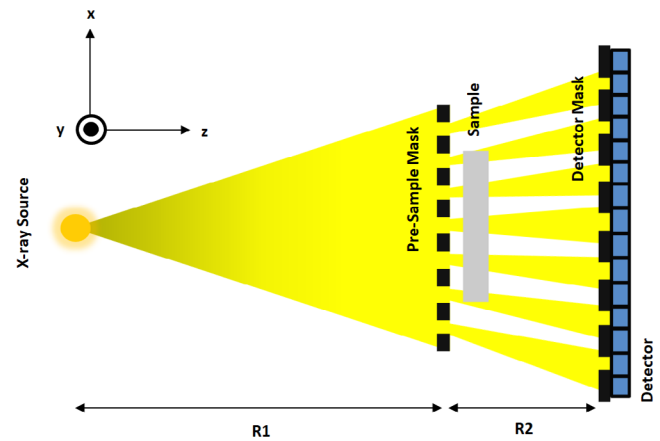


**Figure 1.** Schematic representation of the laboratory-based edge-illumination x-ray imaging system used in this experiment.

To extract the dark-field signal in EI, we start by measuring the illumination curve (IC) without a sample in place. The IC is the intensity modulation observed at the detector when one of the masks is scanned transversally (along the  $x$ -axis in figure 1). Figure 2 schematizes the measurement method and highlights some key physical quantities of the IC. Following the introduction of a sample, the sample and the sample mask are moved rigidly with respect to the stationary detector/detector mask assembly (system dithering in figure 2(a)). The signal in the corresponding detector pixel is measured at each point, and a sample IC is measured. The two curves are fitted with Gaussians and the sample curve ( $I_M(x)$ ) is then compared to the corresponding field curve ( $I_N(x)$ ), without the sample in place.

$$I_N(x) = \frac{t_N}{\sqrt{2\pi\sigma_N^2}} \exp\left[-\frac{(x - \Delta x_N)^2}{2\sigma_N^2}\right] + I_0 \quad (1)$$

$$I_M(x) = t_M \left[ \frac{t_N}{\sqrt{2\pi\sigma_M^2}} \exp\left[-\frac{(x - \Delta x_M)^2}{2\sigma_M^2}\right] + I_0 \right]. \quad (2)$$

The comparison between  $I_M(x)$  and  $I_N(x)$  allows extraction of the attenuation, refraction and dark-field characteristics of the sample on a pixel-by-pixel basis. In particular,  $t_N$ ,  $\Delta x_N$ ,  $\sigma_N$  and  $I_0$  in equation (1) are the area, center, standard deviation and background value of the illumination curve without the sample, respectively. These values depend only on the characteristics of the imaging system, and are used as reference data to retrieve the sample parameters.  $t_M$ ,  $\Delta x_M$  and  $\sigma_M$  in equation (2) are the area ratio (relative area reduction), center and standard deviation of the illumination curve with the sample. These values represent the modification to the IC caused by absorption, refraction and ultra-small-angle x-ray scattering (USAXS) in the sample. It is therefore possible to extract the absorption image  $t_M$ , the differential phase image  $\Delta x_M - \Delta x_N$  and the dark-field (or USAXS) image  $\sigma_M^2 - \sigma_N^2$  of the sample by measuring the illumination curve with and without the sample in place [26–28]. While this procedure yields the above three images sampled at a pitch equal to the detector pixel size, finer sampling pitches can also be accessed

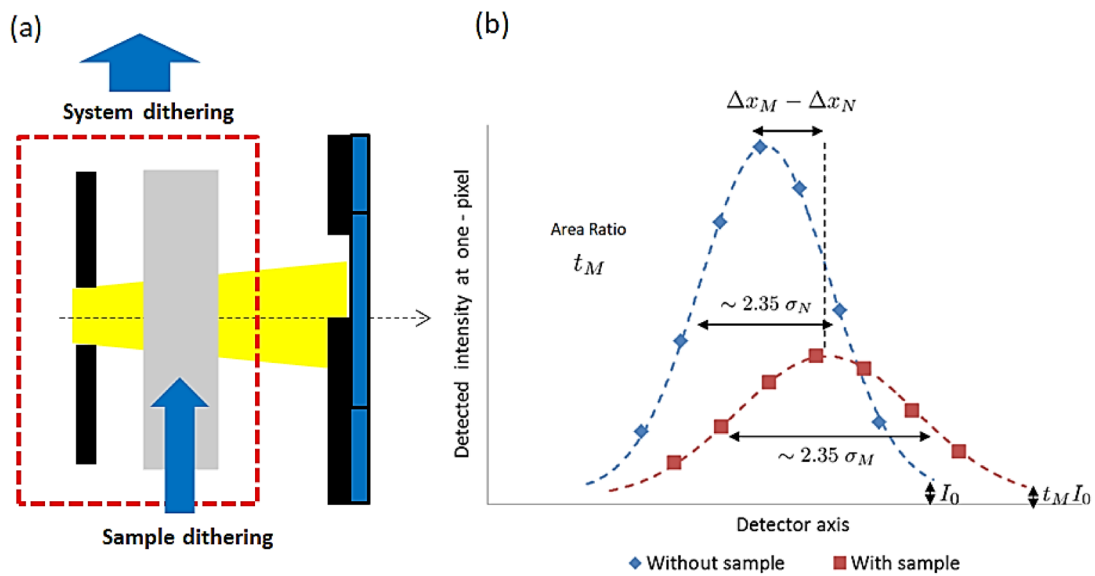


**Figure 2.** (a) Schematization of the approach used to measure the illumination curve with and without the sample. Sample dithering indicates an additional and optional scan which is applied only to the sample, when this is sampled at a pitch finer than the pixel size. (b) Example illumination curves measured with and without the sample in place. The latter induces intensity reduction, lateral shifts and curve broadening that allow extracting attenuation, refraction and dark-field images, respectively.

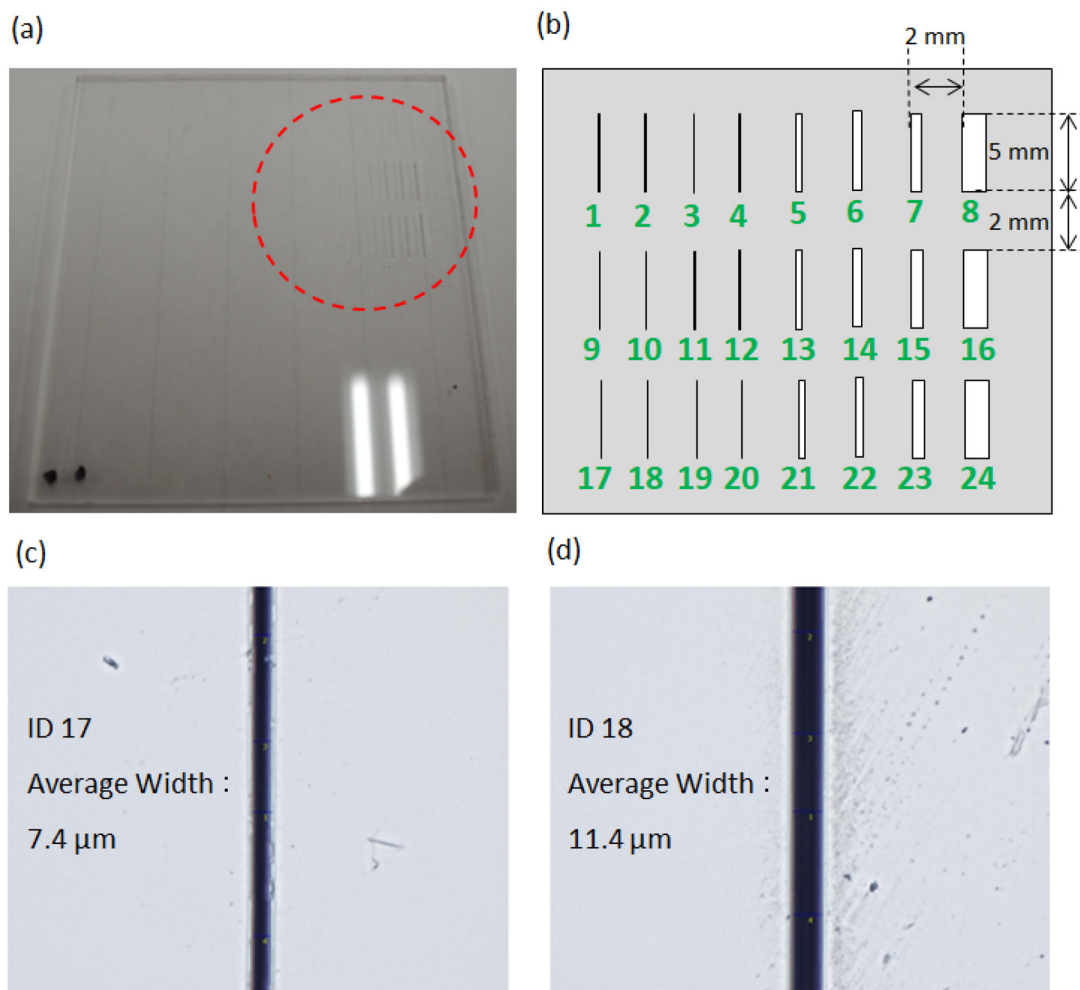


**Figure 3.** (a) Photograph of the sample used, with some of the grooves visible in the top right corner (dashed red circle). (b) Schematic representation of the sample where general dimensions (groove height, separation) are given, and grooves are coded by numbers for ease of reference in the manuscript. (c) and (d) Calibrated optical microscopy images of grooves 17 and 18, respectively, which allowed direct measurement of their average widths.

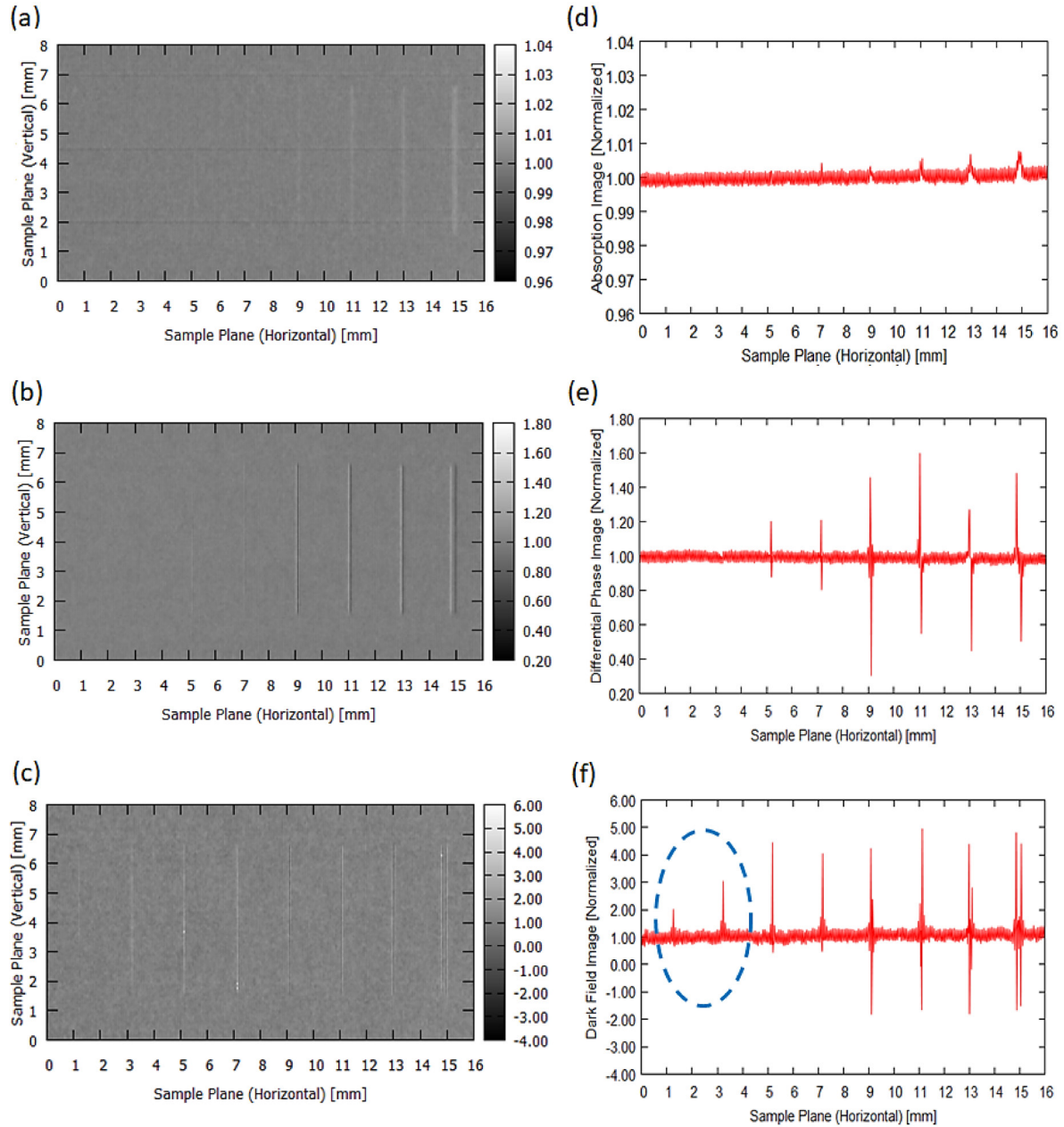


**Figure 4.** Attenuation (a), differential phase (b) and dark-field (c) images of the bottom series of grooves (numbers 17–24). Horizontal profiles were extracted from all images and are reported in panels (d)–(f) for images (a)–(c), respectively. A dashed blue circle in panel (f) highlights the profiles of the thinnest grooves which, despite falling below the resolution limit of the imaging system, and indeed being invisible in the attenuation and differential phase images, are detected through the dark-field channel.

by displacing the sample in sub-pixel steps (sample dithering in figure 2(a)), repeating the above procedure at each step, and interleaving the subsequent acquisitions to obtain the oversampled images. Indeed, four dithering steps were used to produce the images presented below.

The minimum detectable refraction angle depends on the overall number of x-rays contributing to the image formation. A detailed theoretical framework was developed and experimentally validated for the differential phase signal [44] with EI. This sensitivity  $s$ , the minimum resolvable refraction angle, can be expressed as

$$s = \frac{\sqrt{I_N(x)}}{R_2 \sqrt{2t_M t_N} [\rho(x) - \rho(x+a)]} \quad (3)$$

where it is assumed that two images acquired on symmetric positions  $x$  of  $I_N(x)$  (i.e. positions on opposite slopes with the same x-ray intensity) are used to retrieve the refraction angle.  $\rho$  is the shape of the beamlets at the detector mask and  $a$  is the aperture size. The term  $[\rho(x) - \rho(x+a)]$  expresses the change of the beamlet intensity across the aperture. Obtaining an equivalent expression for the dark-field signal is not trivial, and goes beyond the scope of the present manuscript. As



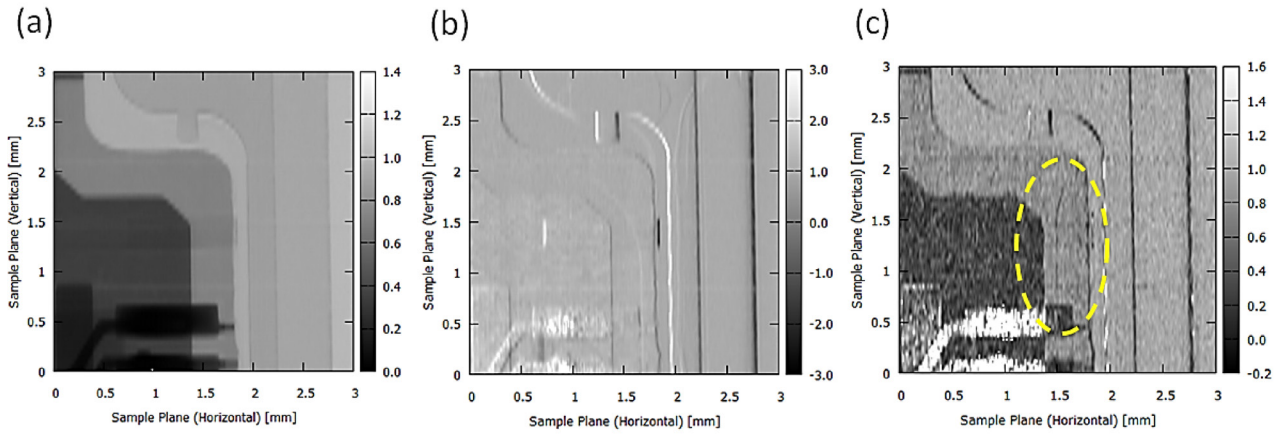


**Figure 5.** Attenuation (a), differential phase (b) and dark-field (c) images of a part of the cracked SD card. The dashed yellow circle in (c) shows the detected cracked part through only the dark-field channel.

well as depending on concentration [39] and size [41] of the sub-pixel features, there is evidence that the signal intensity also depends on their shape and orientation [45]. Here we are experimentally showing that the dark-field signal allows the detection of isolated features that are undetected by both the attenuation and the differential phase channels, all other imaging conditions being the same.

### 3. Experiment

We focused on a sample that was specifically designed to assess the ability of the dark-field image to detect individual sub-pixel features that are invisible to the other contrast channels. This consists of a series of microgrooves carved in a 2 mm thick acrylic substrate as shown in figure 3. Figure 3(a) is a photograph of the sample, with the widest grooves in the top right corner (dashed red circle). Figure 3(b) is a schematic providing the height and spacing between grooves, and the number coding we will use to refer to their individual widths and depths. The depth of all grooves in the top group (1–8) is  $10\ \mu\text{m}$ , and their widths range from  $6\ \mu\text{m}$  (groove 1, far left) to  $200\ \mu\text{m}$  (groove 8, far right). The nominal widths of the intermediate grooves are  $10\ \mu\text{m}$ ,  $14\ \mu\text{m}$ ,  $17\ \mu\text{m}$ ,  $50\ \mu\text{m}$ ,  $77\ \mu\text{m}$  and  $100\ \mu\text{m}$  for grooves 2–7, respectively. The grooves in the middle (9–16) and bottom (17–24) groups have the same width distribution, but depths of  $50\ \mu\text{m}$  and  $100\ \mu\text{m}$ , respectively. Figures 3(c) and (d) are optical microscope images of grooves 17 and 18, respectively, in which their widths were measured as  $7.4\ \mu\text{m}$  and  $11.4\ \mu\text{m}$ , respectively. Likewise, when grooves 19–24 were measured they were shown to diverge slightly from the nominal values reported above, with measured values of  $16.6\ \mu\text{m}$ ,  $20\ \mu\text{m}$ ,  $51\ \mu\text{m}$ ,  $85\ \mu\text{m}$ ,  $109\ \mu\text{m}$  and  $200\ \mu\text{m}$ , respectively. All microgrooves were fabricated using excimer laser technology.

This sample was imaged with the imaging system and parameters outlined above, and the attenuation, differential phase and dark-field images were extracted by using the fitting procedure of equations (1) and (2). Details from the resulting images of grooves 17–24 (corresponding to the entire bottom line of the phantom) are shown in panels (a)–(c) of figure 4,

respectively. Horizontal profiles were extracted from each image, and these are reported in panels (d)–(f) for attenuation, differential phase and dark field, respectively.

### 4. Discussion and conclusion

As per the model described in [42], we expect the spatial resolution of the EI system used to be of the order of  $20\ \mu\text{m}$ , which corresponds approximately to the projected focal spot and is slightly smaller than the apertures in the pre-sample mask. However, we note that this model is useful for determining whether two adjacent features can still be detected as separate by the imaging system and, as such, it does not apply directly to the detection of isolated objects, which rather depends on the signal intensity they create. While this can be calculated for attenuation and differential phase features, its determination in the dark-field case is made more complicated by its dependence on multiple parameters as discussed above. However, we note here that the visualization of finer details extends further in the dark-field image, compared to those for attenuation and differential phase, which were extracted from the same dataset and therefore obtained with the same x-ray exposure and sampling rate. This can be seen in figure 4(c) and even more clearly in the plot of figure 4(f). The dashed blue circle highlights the additional details detected. Indeed, these details (17 and 18 in the scheme of figure 3(b)) have (measured) widths of  $7.4\ \mu\text{m}$  and  $11.4\ \mu\text{m}$ , respectively, both significantly smaller than both the projected focal spot and the aperture in the pre-sample mask. We find these results might suggest new application opportunities for the dark-field imaging method. Alongside its ability to provide a signal proportional to the average concentration of sub-pixel structures, which was reported before [19, 36–41], we observe here that dark-field can also detect single, isolated features below the resolution limits of the imaging system, which are not picked up by the phase or attenuation contrast channels. A combination of detail dimensions and signal strength is what pushes a given feature above the detectability limit, as made evident by the fact that the same fine features were not detected for the shallower grooves despite them having

the same width. A point to note is that, given sufficient x-ray statistics, it is possible that finer details would progressively also become detectable in the differential phase and attenuation images. However the key point here is the demonstration that the detectability threshold is pushed further in the dark-field channel at the same x-ray statistics. We also note here that the use of dithering (see section (2)) is helping this increased detectability by providing a finer sampling pitch. However this procedure has been applied to all contrast channels in the same way, and yet more features are detectable in the dark-field image. This property may offer an opportunity to detect isolated defects or micro-cracks on a scale that would not be accessible to other imaging modalities with the same x-ray statistics (exposure and/or scan time), with potential applications in non-destructive testing. As a practical example we report the images of a cracked SD card. Figures 5(a)–(c) are attenuation, differential phase and dark-field images of the sample. The dashed yellow circle in figure 5(c) highlights the crack that can be detected only through the dark-field channel. Through comparison with the groove results of figure 4, one may argue that the crack could be expected to be smaller than 20  $\mu\text{m}$  as it is detected by the dark-field channel but not by the differential phase one. This is a specific and practical result, which shows the potential for more general applications in the life and physical sciences, and non-destructive inspection applications.

## Acknowledgments

The authors would like to thank Mr Atsushi Yamada (Optical Research Laboratory, Nikon Corporation) and team members at the Department of Medical Physics and Biomedical Engineering, UCL. This project was part-supported by the UK Engineering and Physical Sciences Research Council Grant No. EP/I021884/1. ME is supported by the Royal Academy of Engineering under the RAEng Research Fellowships scheme. AO is supported by the Royal Academy of Engineering under the Chairs in Emerging Technologies scheme.

## ORCID iDs

Marco Endrizzi  <https://orcid.org/0000-0002-7810-2301>

## References

- [1] Teague M R 1982 *J. Opt. Soc. Am.* **72** 1199
- [2] Teague M R 1983 *J. Opt. Soc. Am.* **73** 1434
- [3] Snigirev A, Snigireva I, Kohn V, Kuznetsov S and Schelokov I 1995 *Rev. Sci. Instrum.* **66** 5486
- [4] Wilkins S W, Gureyev T E, Gao D, Pogany A and Stevenson A W 1996 *Nature* **384** 335
- [5] Gureyev T E and Wilkins S W 1998 *J. Opt. Soc. Am. A* **15** 3
- [6] Guigay J P, Langer M, Bolstel R and Cloetens P 2007 *Opt. Lett.* **32** 12
- [7] Bonse U and Hart M 1965 *Appl. Phys. Lett.* **7** 99
- [8] Momose A 1995 *Nucl. Inst. Meth. Phys. Res. A* **352** 622
- [9] Yoneyama A, Hyodo K and Takeda T 2013 *Appl. Phys. Lett.* **103** 204108
- [10] Davis J, Gao D, Gureyev T E, Stevenson A W and Wilkins S W 1995 *Nature* **373** 595
- [11] Chapman D, Thomlinson W, Johnston R E, Washburn D, Pisano E, Gmür N, Zhong Z, Menk R, Arfelli F and Sayers D 1997 *Phys. Med. Biol.* **42** 2015
- [12] Zhong Z, Thomlinson W, Chapman D and Sayers D 2000 *Nucl. Inst. Meth. Phys. Res. A* **450** 556
- [13] Dilmanian F A, Zhong Z, Ren B, Wu X Y, Chapman L D, Orion I and Thomlinson W C 2000 *Phys. Med. Biol.* **45** 933
- [14] Koyama I, Momose A, Wu J, Lwin T T and Takeda T 2005 *Japan. J. Appl. Phys.* **44** 8219
- [15] Momose A, Kawamoto S, Koyama I, Hamaishi Y, Takai K and Suzuki Y 2003 *Japan. J. Appl. Phys.* **42** L866
- [16] Pfeiffer F, Weitkamp T, Bunk O and David C 2006 *Nat. Phys.* **2** 258
- [17] Pfeiffer F, Bech M, Bunk O, Eikenberry E F, Brönnimann C, Grünzweig C and David C 2008 *Nat. Mater.* **7** 134
- [18] Wang Z T, Kang K J, Huang Z F and Chen Z Q 2009 *Appl. Phys. Lett.* **95** 094105
- [19] Yashiro W, Teui Y, Kawabata K and Momose A 2010 *Opt. Express* **18** 16890
- [20] Uehara M, Yashiro W and Momose A 2013 *J. Appl. Phys.* **114** 134901
- [21] Yashiro W and Momose A 2014 *Japan. J. Appl. Phys.* **53** 05FH04
- [22] Yashiro W and Momose A 2015 *Opt. Express* **23** 9233
- [23] Olivo A and Speller R 2007 *Appl. Phys. Lett.* **91** 074106
- [24] Olivo A and Speller R 2007 *Phys. Med. Biol.* **52** 6555
- [25] Olivo A and Speller R 2008 *Phys. Med. Biol.* **53** 6461
- [26] Endrizzi M, Diemoz P C, Millard T P, Louise Jones J, Speller R D, Robinson I K and Olivo A 2014 *Appl. Phys. Lett.* **104** 024106
- [27] Endrizzi M, Diemoz P C, Hagen C K, Millard T P, Vittoria F A, Wagner U H, Rau C, Robinson I K and Olivo A 2014 *IEEE Nuclear Science Symp. and Medical Imaging Conf.* p 7431019
- [28] Endrizzi M, Murat B I S, Fromme P and Olivo A 2015 *Compos. Struct.* **134** 895
- [29] Modregger P, Cremona T P, Benarafa C, Schittny J C, Olivo A and Endrizzi M 2016 *Sci. Rep.* **6** 30940
- [30] Bravin A, Coan P and Suortti P 2013 *Phys. Med. Biol.* **58** R1
- [31] Olivo A and Castelli E 2014 *Riv. Nuovo Cimento* **37** 467
- [32] Endrizzi M 2018 *Nucl. Instrum. Meth. Phys. Res. A* **878** 88
- [33] Endrizzi M, Vittoria F A, Kallon G, Basta D, Diemoz P C, Vincenzi A, Delogu P, Bellazzini R and Olivo A 2015 *Opt. Exp.* **23** 16473
- [34] Millard T P, Endrizzi M, Ignatyev K, Hagen C K, Munro P R T, Speller R D and Olivo A 2013 *Rev. Sci. Instrum.* **84** 083702
- [35] Olivo A et al 2001 *Med. Phys.* **28** 1610
- [36] Rigon L, Besch H J, Arfelli F, Menk R H, Heitner G and Plotow-Besch H 2003 *J. Phys. D: Appl. Phys.* **36** A107
- [37] Revol V, Plank B, Kaufmann R, Kottler C and Neels A 2013 *NDT and E Int.* **58** 64
- [38] Lynch S K, Pai V, Auxier J, Stein A F, Bennett E E, Kemble C K, Xiao X, Lee W-K, Morgan N Y and Wen H 2011 *Appl. Opt.* **50** 4310

- [39] Millard T P, Endrizzi M, Rigon L, Arfelli F, Menk R H, Owen J, Stride E and Olivo A 2013 *Appl. Phys. Lett.* **103** 114105
- [40] Gkoumas S, Villanueva-Perez P, Wang Z, Romano L, Abbis M and Stampanoni M 2016 *Sci. Rep.* **6** 35259
- [41] Modregger P, Kagias M, Irvine S C, Brönnimann R, Jefimovs K, Endrizzi M and Olivo A 2017 *Phys. Rev. Lett.* **118** 265501
- [42] Diemoz P C, Vittoria F A and Olivo A 2014 *Opt. Exp.* **22** 15514
- [43] Ignatyev K, Munro P R T, Speller R D and Olivo A 2011 *Rev. Sci. Instrum.* **82** 073702
- [44] Diemoz P C, Hagen C K, Endrizzi M and Olivo A 2013 *Appl. Phys. Lett.* **103** 244104
- [45] Yashiro W, Harasse S, Kawabata K, Kuwabara H, Yamazaki T and Momose A 2011 *Phys. Rev. B* **84** 094106